A series of climate oscillations around 8.2 ka BP revealed through multi-proxy speleothem records from North China

Pengzhen Duan[1], Hanying Li[2], Zhibang Ma[3], Jingyao Zhao[2], Xiyu Dong[2], Ashish Sinha[4], Peng Hu[5,6], Haiwei Zhang[2], Youfeng Ning[2], Guangyou Zhu[1], Hai Cheng[2,7,8]

[1]Research Institute of Petroleum Exploration and Development, PetroChina, Beijing, China

[2]Institute of Global Environmental Change, Xi'an Jiaotong University, Xi'an, China

[3]Key Laboratory of Cenozoic Geology and Environment, Institute of Geology and Geophysics, Chinese Academy of Sciences, Beijing, China

[4]Department of Earth Science, California State University, Dominguez Hills, Carson, USA

[5]Yunnan Key Laboratory of Meteorological Disasters and Climate Resources in the Greater Mekong Subregion, Yunnan University, Kunming 650091, China

[6]Department of Atmospheric Sciences, Yunnan University, Kunming 650500, China

[7]State Key Laboratory of Loess and Quaternary Geology, Institute of Earth Environment, Chinese Academy of Sciences, Xi'an, China

[8]Key Laboratory of Karst Dynamics, MLR, Institute of Karst Geology, CAGS, Guilin, China

Correspondence to: Hanying Li (hanyingli@xjtu.edu.cn) and Hai Cheng (cheng021@xjtu.edu.cn)

Abstract. The 8.2 ka event has been extensively investigated as a remarkable single event, but rarely considered as a part of multi-centennial climatic evolution. Here, we present absolutely dated speleothem multi-proxy records spanning 9.0–7.9 ka BP from Beijing in North China, near the northern limit of the East Asian summer monsoon (EASM) and thus sensitive to climate change, to provide evidence for the intensified multi-decadal climatic oscillations since 8.52 ka BP. Three extreme excursions characterized by inter-decadal consecutive δ^{18}O excursions exceeding $\pm 1\sigma$ are identified from 8.52 ka BP in our speleothem record. The former two are characterized by enriched ^{18}O at ~8.50 and 8.20 ka BP, respectively, suggesting a prolonged arid event, which is supported by the positive trend in δ^{13}C values, increased trace element ratios, and lower growth rate. Following the 8.2 ka event, an excessive rebound immediately emerges in our δ^{18}O and trace element records but moderate in the δ^{13}C, probably suggesting pluvial conditions and nonlinear response of the local ecosystem. Following two similar severe droughts at 8.50 and 8.20 ka BP, the different behavior of δ^{13}C suggests the recovering degree of resilient ecosystem responding to different rebounded rainfall intensity. A comparison with other high-resolution records suggests that the two droughts-one pluvial patterns between 8.52 and 8.0 ka BP are of global significance instead of a regional phenomenon, which is causally linked to the slowdown and acceleration of the Atlantic Meridional Overturning Circulation that was further dominated by the freshwater injections in the North Atlantic.

1 Introduction

The overall warming during 9.0–7.9 ka BP (thousand years before present, where the present is 1950 CE) was punctuated by several inter-decadal to centennial climate fluctuations in the Northern Hemisphere (NH). The 8.2 ka event, as the most prominent abrupt cold event registered in the Greenland ice core records within the Holocene (Thomas et al., 2007), has been widely revealed by a large number of marine and terrestrial archives and dated to occur between 8.3–8.0 ka BP with a duration of 150–200 years (Figure S1) (e.g., Alley et al., 1997; Thomas et al., 2007; Kobashi et al., 2007; Cheng et al., 2009; Liu et al., 2013; Morrill et al., 2013; Duan P et al., 2021).

With deeper investigation, the "cold event" at 8.2 ka BP is evidenced likely to be a part of larger "set" of cold climate anomalies between 8.6 and 8.0 ka BP (e.g., Rohling and Pälike, 2005). According to marine records, the freshwater drainage(s) of proglacial Lakes Agassiz-Ojibway (LAO) into the North Atlantic, which has commonly been thought to trigger the 8.2 ka event (e.g., Alley et al., 1997; Barber et al., 1999) through weakening the Atlantic meridional overturning circulation (AMOC) and resultant global impact, is supposed to separate into two stages (Ellison et al., 2006; Roy et al., 2011; Godbout et al., 2019, 2020) or multiple outbursts (e.g., Teller et al., 2002; Kleiven et al., 2008; Jennings et al., 2015). The first pulse of freshwater may have induced the freshening of the North Atlantic at 8.55–8.45 ka BP (Lochte et al., 2019), the abrupt sea level jump (Tornqvist and Hijma, 2012; Lawrence et al., 2016), the detrital carbonate peak at ~8.6 ka (Jennings et al., 2015), and deposition of a red-sediment bed in Hudson Strait at ~8.26–8.69 ka BP (Kerwin, 1996; Lajeunesse and St-Onge, 2008). The superimposed effect of two or more successive freshwater drainages, or probably coupled with meltwater flux from the ice sheet (Morrill et al., 2014; Matero et al., 2017), finally led to severe and dramatic cooling events in the NH (Teller et al., 2002; Ellison et al., 2006). This is consistent with the view that the 8.2 ka event commenced at ~8.5 ka BP and persisted until ~8.0 ka BP (Rohling and Pälike, 2005) with more than one multi-decadal or centennial perturbations (e.g., Daley et al., 2009; Domínguez-Villar et al., 2009; Tan et al., 2020; Duan W et al., 2021). However, some terrestrial records, such as the Greenland ice cores (Thomas et al., 2007) and European lake sediments (von Grafenstein et al., 1999; Andersen et al., 2017), only documented a remarkable climate event at ~8.2 ka BP, whereas the counterpart to the preceding perturbation is not registered.

On the other hand, the multi-decadal or centennial perturbations aforementioned trended not only to the cold and dry direction in the NH, but also extremely warm and humid condition that has been evidenced in the immediate aftermath of the 8.2 ka event (Andersen et al., 2017; Duan P et al., 2023). In particular, the post-event excessive rebound suggests a major pluvial episode prevailing across a large part of North China (Duan P et al., 2023). However, only one proxy, speleothem $\delta^{18}O$ (Duan P et al., 2023), is insufficient and thus multi-proxy evidences about the overshoot is necessary, especially from the Asian summer monsoon (ASM) domain where the climate change has a fast atmospheric teleconnection with the high-latitude North Atlantic (Cheng et al., 2020; 2022), to complement our understanding on the dynamics of rapid climatic changes, their underlying mechanisms, and the local ecosystem response.

In the context of high-emission greenhouse gas nowadays, the melted Greenland ice sheet will inject huge amount of freshwater into the North Atlantic in the next millennium, which is analogous to the sea level rising scenario during 9.0–7.9 ka BP (e.g., Aguiar et al., 2020). Therefore, it is important to elucidate the climate variations in response to the freshwater injections in the past to provide a potential analogy for future behavior, especially in North China where

70 the ecosystem and economic development are highly dependent on hydroclimatic changes. Importantly, our study area

71 is located near the northern fringe of the East Asian summer monsoon (EASM), thus sensitively responding to the

72 variations of EASM intensity (Duan et al., 2014; Li et al., 2017; Ma et al., 2012). Here we provide high temporal

73 resolution speleothem multi-proxy records, including $\delta^{18}O$, $\delta^{13}C$, Mg/Ca, Sr/Ca, and Ba/Ca, from Beijing in North

74 China to reconstruct the hydroclimatic variations over the Circum-Bohai Sea Region (CBSR) between 9.0–7.9 ka BP.

75 Two climate anomalous events occurring before and at 8.2 ka BP, as well as a post-8.2 ka rebound, are investigated

76 to show the general climate pattern around the abrupt cold event from its triggering, response, and ensuing feedback

77 and further examine the relationship between the ASM and the North Atlantic.

78 2 Materials and Methods

79 2.1 Regional settings and modern climatology

80 Situated at ~60 km southwest of Beijing in North China, the Huangyuan Cave (39°42′ N, 115°54′ E, altitude 610 m

81 above sea level) is developed in a Middle Proterozoic dolomite and adjacent to Kulishu (39°41′ N, 115°39′ E) and

82 Shihua (39°47′ N, 115°56′ E) Caves (Figure S1). The vegetation above the cave is dominated by secondary-growth

83 deciduous broadleaf trees and shrubs (Ma et al., 2012; Duan et al., 2014). According to the meteorological station's

84 observed data between 1998 and 2010 CE, the average annual air temperature and precipitation in the study area are

85 12.2 °C and 540 mm, respectively, with cold dry winters and warm wet summers (Figure 1). The regional precipitation

86 is highly seasonal and mainly concentrates on the summer season with more than 420 mm occurring from June to

87 September. It has been demonstrated (Duan et al., 2016; Li et al., 2017; Duan P et al., 2023) that the summer

88 precipitation $\delta^{18}O$ ($\delta^{18}O_p$) is negatively correlated with the summer rainfall amount over the study area and positively

89 correlated with $\delta^{18}O_p$ over almost the entire EASM domain, the latter of which is normally related to the EASM

90 intensity.

91 Speleothem BH-2, collected from Huangyuan Cave, is ~17 cm in length and ~5 cm in width (Figure 2a). The

92 candlestick shape of speleothem without macroscopic bias of the growth axis signifies that it was deposited under

93 relatively stable conditions (Baker et al., 2007). The $\delta^{18}O$ results for the section of 15–48 mm from the top of the

94 sample, corresponding to 8.38–8.06 ka BP, have been reported in previous investigation (Duan P et al., 2023). In this

95 study, the multi-proxy results of the entire sample are presented that spans 9.0–7.9 ka BP.

96 2.2 ^{230}Th dating, stable isotope, and trace element analysis

97 A total of 22 ^{230}Th dates (Table S1) were performed at University of Minnesota, USA, using Thermo-Finnigan

98 Neptune multi-collector inductively coupled plasma mass spectrometers (MC-ICP-MS, Thermo Scientific). The

99 methods are described in detail in Cheng et al. (2013). We followed standard chemistry procedures to separate uranium

100 and thorium for instrument analysis (Edwards et al., 1987). A triple-spike (^{229}Th-^{233}U-^{236}U) isotope dilution method

101 was employed to correct instrumental fractionation and determine U/Th isotopic ratios and concentrations.

102 Uncertainties in U/Th isotopic data were calculated offline at 2σ level. The chronology for the section of 15 to 48 mm

103 is based on the combination of annual banding and ^{230}Th dates as reported in previous study (Duan P et al., 2023).

104 The stable oxygen and carbon isotopes ($\delta^{18}O$ and $\delta^{13}C$) of speleothem BH-2 were determined on a Thermo-Scientific
105 MAT-253 isotope ratio mass spectrometer equipped with an online carbonate device (Kiel IV) at the Institute of
106 Geology and Geophysics, Chinese Academy of Sciences and Isotope Laboratory of Xi'an Jiaotong University. The
107 powdered subsamples weighing ~30 μg were drilled along the central growth axis using a Micromill device and then
108 reacted with ~103 % phosphoric acid at 70 °C. The stable oxygen and carbon isotopic compositions of the generated
109 CO_2 gas were measured with working CO_2 standard gas whose values have been calibrated by two international
110 standards named NBS18 and IAEA-603. All results are reported as the per mil deviation relative to the Vienna Pee
111 Dee Belemnite (VPDB). The reported precision of both $\delta^{18}O$ and $\delta^{13}C$ at 1σ level is better than 0.1 ‰.

112 Trace element ratios (Mg/Ca, Sr/Ca, Ba/Ca), of which the intensity ratio of emission lines are 285.2 (Mg), 407.8 (Sr),
113 and 493.4 (Ba) nm relative to 373.7 nm (Ca), were measured using Laser Induced Breakdown Spectroscopy (LIBS)
114 following the detailed description in Li et al. (2018). In brief, analyses were performed by pulsing and focusing
115 yttrium-aluminum-garnet-Nd laser beam to 0.1 mm. Emitted plasma from the stalagmite surface was collected by
116 optical fibers and sent to a four-passage spectrometer (Ocean Optics MX500+) to obtain a spectrum within the 200-
117 to 580-nm range. These data were determined through the intensity of characteristic spectral line for each element,
118 and then the intensity ratio of each trace element signal to Ca element was calculated and output as the final result for
119 each point. The obtained record is the median intensity ratio based on 20 pulses at each sampling site after 5 laser
120 shots for pre-cleaning the surface. The measurements were performed continuously along the speleothem's growth
121 axis at 0.3 mm increment and a total of 565 data were obtained. The accuracy of data was ensured through the excellent
122 replicability between two-time measurements instead of inset standard materials because of the overwhelming amount
123 of Ca relative to trace elements in speleothem. The original spectral data were processed using an interface created in
124 MATLAB (2020a). The typical standard deviation for the average intensity ratio is less than 0.02 (without unit).

125 **3 Results**

126 **3.1 ^{230}Th dates and age model**

127 The ^{230}Th dating results of the BH-2 are presented in Table S1, which shows that the BH-2 covers the interval between
128 9.0 and 7.9 ka BP. Almost all dates are in stratigraphic order within uncertainties. The average dating uncertainty is ±
129 57 years at 2σ level. For the period from 8.25 to 8.11 ka BP, we present the speleothem record from Duan P et al.
130 (2023), which is based on the combination of the annual lamina counting and ^{230}Th dates. In addition, here we use an
131 updated chronology of the BH-2 based on the Stalage algorithm (Scholz and Hoffmann, 2011), which includes eleven
132 additional ages from the remnant sections (Figure 2b and S2). In detail, the fitted age and error for each annual band
133 between 16 and 43 mm were obtained based on the least square method (Duan et al., 2023). To establish a
134 consecutively composite chronology for the entire record, all these fitting results in 16–43 mm (corresponding to
135 8.077–8.324 ka BP) with uncertainties and the other fifteen ^{230}Th dates in the remnant study section were input to
136 Stalage algorithm. In this way, the seven ^{230}Th dates drilled from 16–43 mm were only used in the layer band counting
137 procedure but not the Stalage age model. The output results of Stalage were adopted as the reconstructed chronology
138 for isotope and trace element records.

3.2 Stable isotopic compositions and growth rate

The BH-2 record contains 663 pairs of $\delta^{18}O$ and $\delta^{13}C$ data with a mean temporal resolution of ~1.6 years. The $\delta^{18}O$ values range from -7.1 ‰ to -11.5‰ with a mean of -9.3 ‰ and $\delta^{13}C$ values vary from -8.0 ‰ to -12.1 ‰ with an average value of -10.2 ‰ (Figures 2d and 2e). It can be seen that the $\delta^{13}C$ profile follows the same general patterns as the $\delta^{18}O$ ($r = 0.63$, $p < 0.01$). Compared to the later stage, although some fluctuations are included, the $\delta^{13}C$ and $\delta^{18}O$ profiles are relatively invariable before 8.52 ka BP. In contrast, the $\delta^{18}O$ record exhibits a remarkable positive shift at ~8.52–8.48 ka BP, during which period the $\delta^{13}C$ record shifts less prominently to the positive direction but with a fluctuating increasing trend. The rebound from the positive shift of $\delta^{13}C$ and $\delta^{18}O$ profiles is followed by a less variable episode spanning 8.48–8.26 ka BP. Afterward, as the most remarkable feature, both records show extremely positive excursions spanning ~8.26–8.14 ka BP (Figure 2). The positive anomaly is followed by a shift to the opposite extreme to reach the most negative stage in the $\delta^{18}O$ record during 8.14–8.05 ka BP, which is not conspicuous in the $\delta^{13}C$ record.

The growth rate of the BH-2 established based on the reconstructed chronology (Figures 2c and S2) is highly variable with two peaks of more than 0.8 mm/year at 8.85 and 8.51 ka BP. It is apparent that speleothem BH-2 was contiguously deposited without visible growth hiatus and the growth rate during 8.51–8.16 ka BP (< 0.15 mm/year) is apparently lower relative to other intervals (> 0.15 mm/year on average). Specifically, there are obvious transitions from higher to lower growth rates at ~8.51 ka BP and in the opposite trend at ~8.16 ka BP.

3.3 Trace element ratios

The trace element ratio records of two-time measurements are replicable, suggesting the robustness of LIBS technique (Figure S3). As can be seen, the signals in the records are quite variable (Figures 2 and S3). The correlation coefficients (r) for pairs of Mg/Ca and Sr/Ca, Mg/Ca and Ba/Ca, and Sr/Ca and Ba/Ca, are 0.24 ($p<0.01$), 0.49 ($p<0.01$), and 0.47 ($p<0.01$), respectively. Similar to $\delta^{18}O$ and $\delta^{13}C$ records, all of the Mg/Ca, Sr/Ca, and Ba/Ca records display positive excursions at ~8.50 and 8.20 ka BP despite the relative ambiguity of the former one in the Sr/Ca and the latter one in the Ba/Ca, respectively. Besides, there is another more positive excursion at ~ 8.88~8.82 ka BP in the Ba/Ca ratio record, which is absent in the other two records. After principal component analysis of the three records, the excursions at ~8.50 and 8.20 ka BP are especially conspicuous (Figure 2f). Different from the $\delta^{18}O$ and $\delta^{13}C$ variability, the PC1 result of trace element ratio fluctuates frequently with considerable magnitude and show a general decreasing trend before 8.52 ka BP. In the duration of 8.52–8.48 ka BP, it exhibits a fluctuating positive trend and a rapid rebound. Afterwards, the values remain relatively stable until ~8.23 ka BP when another positive excursion commences. In this excursion, the PC1 values culminate at ~8.12 ka BP followed by a rapid rebound which indicates the termination of this excursion. The values remain relatively stable after 8.10 ka BP.

4 Discussion

4.1 Proxy interpretations

The replication test of $\delta^{18}O$ records between the BH-2 from Huangyuan Cave and the KLS12 from nearby Kulishu Cave (Duan W et al., 2021) by using the ISCAM (Intra-site Correlation Age Modeling) algorithm (Fohlmeister, 2012) show significantly positive correlation ($r = 0.62$, $p < 0.05$) during 9.0–7.9 ka BP (Figure S4), strongly suggesting that the influence of kinetic fractionation is likely insignificant and the carbonate deposition process is close to equilibrium (Dorale and Liu, 2009). Hence, the BH-2 $\delta^{18}O$ signals reflect the changes in drip water $\delta^{18}O$ which in turn inherit from $\delta^{18}O_p$ related to the regional hydroclimate variations in general. Notably, the study site is located along the summer monsoon fringe with relatively low annual precipitation, and thus the thermodynamics variations in EASM in the areas can significantly bias the mean annual $\delta^{18}O$ value, e.g., the summer rainfall amount. Indeed, the modern observations (Duan al., 2016) and reanalysis results (Cheng et al., 2019; Zhang et al., 2019; He et al., 2021; Duan P et al., 2023; Zhao et al., 2023) have proved that speleothem $\delta^{18}O$ in the study area can be used as a reliable proxy to indicate the regional precipitation variations and the dynamic changes of the summer monsoon circulation, that is, depleted ^{18}O corresponds to increased rainfall over the study area and strengthened EASM, and vice versa.

Under the equilibrium fractionation conditions, the carbon isotope ratios ($\delta^{13}C$) of speleothem carbonate reflect a mixture of three carbon sources: plant root-respired CO_2 in the soil zone, atmospheric CO_2, and dissolution of bedrock carbonate (McDermott, 2004), in which the plant-related CO_2 is the most important for the variability of the speleothem $\delta^{13}C$ (Fairchild et al., 2006; Li Y et al., 2020). It has been suggested that changes in the density of vegetative cover and biomass activity exert a critical impact on the speleothem $\delta^{13}C$ variations in the study region, instead of the relative ratio of C3 (woody taxa) and C4 (grasses) plants (Duan et al., 2014). This is consistent with our observation that the $\delta^{13}C$ values of speleothem BH-2 fall between -8 and -12 ‰, which is within the typical range for the C3-dominant plant coverage (McDermott, 2004; Fairchild et al., 2006). Although climate-induced changes in the karst system, like pCO_2 degassing, water infiltration, and prior calcite precipitation (PCP) could also contribute to the $\delta^{13}C$ changes (Fairchild and Treble, 2009; Li et al., 2020), the significant covariance of $\delta^{13}C$ and $\delta^{18}O$ in the BH-2 and minor effect of kinetic fractionations as aforementioned, as well as the unbiased $\delta^{18}O$ signal inherited from precipitation strongly suggest that the density of vegetative cover, the biomass activity, and the vadose of seepage solution dominated by regional hydroclimatic conditions could play a crucial role in the decadal to centennial scale variations of $\delta^{13}C$ in speleothem BH-2. In addition to rainfall amount, the impact of temperature variations are non-negligible for the growth of plant and biomass activity as well.

The influence of PCP can be inferred from trace element concentrations such that strong (weak) PCP normally induces a high (low) trace element content relative to the calcium in the speleothem calcite (Johnson et al., 2006; Fairchild and Treble, 2009). In general, higher trace element ratio values indicate overall drier conditions when reduced infiltration and increased residence time in the epikarst above the cave favors faster CO_2 degassing and PCP, inducing relatively higher trace element content in the cave drip-water due to the preferential loss of Ca^{2+} along the deposition path; the opposite processes occur in wetter conditions (e.g., Cruz et al., 2007; Griffiths et al., 2010; Zhang et al., 2018). On the other hand, water-rock interaction may have been enhanced in the aquifer during direr conditions because of the prolonged residence time of fluid in the path way, which tends to favor the leaching of Mg and Sr

207 element from the dolomite host rock (Fairchild et al., 2000) and eventually leads the two elements to enrichment in
208 dripwater, and hence speleothem. Apparently, both above two mechanisms indicate the trace element ratios can be
209 used as a reliable proxy of local wetness conditions. Regarding the speleothem growth rate, the sharp drops and
210 persistent lower values in this proxy corresponding to major positive $\delta^{18}O$ and $\delta^{13}C$ excursions signify that it most
211 likely was controlled by a sufficient or insufficient supply of drip water, and hence the local rainfall amount (e.g.,
212 Polyak et al., 2004; Banner et al., 2007).

213 The discrepancy among proxies could suggest that different factors exert influence on these signals in the meteoric
214 water-cave aquifer-drip water-carbonate precipitation processes. One thing should be emphasized here is that although
215 speleothem both $\delta^{18}O$ and trace element PC1 in this study is interpreted to reflect local rainfall amount, it doesn't
216 mean that these two parameters are linearly related. In other words, strict correlation between two proxies cannot be
217 always expected. In addition, the $\delta^{18}O$ from original precipitation can be elevated in the processes from the earth
218 surface to seepage due to possible evaporation loss, broadly resemble the impact of PCP on trace element ratios. Due
219 to the resilience of ecosystem in some degree, plant cover and biomass activity could exhibit more stable patterns
220 relative to the $\delta^{18}O$ and PC1 proxies and thus delayed or muted signals. Therefore, in this study, proxies are interpreted
221 as followings: the speleothem $\delta^{18}O$ variations mainly reflect the change of large scale atmospheric circulation and are
222 consistent over the entire EASM region in pattern; trace element ratios mainly come from the change of precipitation
223 amount which further is related to, instead of strictly follow, the atmospheric circulation pattern; the speleothem $\delta^{13}C$
224 values record the fluctuation of vegetation cover and biomass activity dominated by hydroclimatic conditions. In
225 summary, the broad similarity of multi-proxies ($\delta^{18}O$, $\delta^{13}C$, trace element ratios, and growth rate) in speleothem BH-
226 2 lends robust support to that all of them record changes in hydroclimatic characteristics (Fairchild and Treble, 2009),
227 that is, the intensity of the EASM and associated rainfall amount presumably dominating the hydroclimatic
228 variabilities over and in the cave in the study area.

229 **4.2 Climate fluctuations between 9.0 and 7.9 ka BP in Beijing**

230 The variability of the BH-2 $\delta^{18}O$ record reveals inter-decadal to multi-decadal dry ($> +1\sigma$) or pluvial ($< -1\sigma$)
231 oscillations from 9.0 to 7.9 ka BP without a distinct long-term trend (Figure 2). One noticeable feature of our $\delta^{18}O$
232 record is a switch from relatively muted to highly variable episodes divided at ~8.52 ka BP, consistent with the absence
233 and dominance of centennial to inter-decadal periodicity before and after 8.52 ka BP, respectively (Figure 2g). The
234 mechanism responsible for this phenomenon could be that, in the background of overall strengthened ASM during
235 9.0-8.0 ka BP, a series of abnormal climate events originating from the northern high latitudes lead to relatively more
236 frequent high-amplitude oscillations in $\delta^{18}O$ profiles and hence more prominent periodicity.

237 The first persistent drought, indicated by positive $\delta^{18}O$ excursion exceeding $+1\sigma$ values for more than 15 years, initially
238 started at 8.52 ka BP and terminated at 8.48 ka BP (8.5 ka event herein). The entire event is characterized by a saw-
239 tooth structure with a dramatic 2.5 ‰ increase within ~20 years and a 2.2 ‰ rebound within 20 years, indicating a
240 fast weakened EASM, and thus reduced precipitation in the study area. This arid condition is supported by the
241 contemporaneous trace element records which show a remarkable positive shift that seems strictly resemble the $\delta^{18}O$
242 record regarding both the shape and duration, pointing to the changed dynamic process in the cave in response to the

243   decreased precipitation water supply. Additionally, the high-to-low transition of growth rate commencing ~8.52 ka

244   BP presumably results from less drip water supply and further in turn reduced precipitation over the cave, marking

245   the start of the EASM weakening. However, the change of vegetation indicated by the δ^{13}C proxy is not immediate.

246   It seems that the increasing δ^{13}C trend begins later than other proxies and only exhibits a short excursion, probably

247   indicating the nonlinear response of vegetation evolution to the hydroclimate change, especially in a short-time climate

248   event. This could be related to the delayed shortage of subground water for plant growth and a muted response of

249   ecological processes to the hydroclimatic variability in a relatively wet context as indicated by low δ^{18}O and trace

250   element values surrounding this excursion (Duan P et al., 2021).

251   Following the end of above arid excursion, another centennial oscillation in much temperate mode persisted to ~8.25

252   ka BP. Subsequently, the BH-2 δ^{18}O exhibited the most remarkable droughts with centennial positive excursion

253   between ~8.26 and 8.11 ka BP, conservatively corresponding to the 8.2 ka event (Duan P et al., 2023). This drought

254   event is also proved in the trace element records via the increased values, in concert with the decreased seepage water

255   and hence enhanced PCP. In detailed structure, these trace element ratio records commonly show prominent positive

256   excursion at ~8.20 and 8.14 ka BP, the latter of which is especially elevated in them. However, the slowly increased

257   pattern in the trace element ratio records from 8.26 to 8.18 ka BP is quite distinct from the δ^{18}O record in which its

258   values dramatically increase in the first 70 years, suggesting the probably nonlinear relationship between regional

259   climate (δ^{18}O) and local hydroclimatic condition (trace element ratios). Moreover, in this event, the δ^{13}C exhibits a

260   prominent positive shift, pointing to the decay of the ecosystem in this severe drought event. It is noteworthy that the

261   variation pattern of δ^{13}C in the 8.2 ka event is more similar to the δ^{18}O relative to the 8.5 ka event. This absence of

262   muted δ^{13}C signal suggests the close relationship between the vegetation and regional hydroclimatic conditions in a

263   long duration and more severe climatic deterioration. Intrigueingly, the lower excursion of growth rate somehow

264   predates other proxies. This inter-proxy discrepancy suggests that there are other potential factors, such as the

265   temperature (Wong et al., 2015), controlling the cave dynamic processes, and the growth rate could be a more

266   qualitative indicator to broadly constrain the hydroclimatic conditions in combination with other proxies.

267   Afterward, the hydroclimatic conditions go to the reverse side of the extreme, manifesting a multi-decadal excessive

268   rebound (i.e., overshoot) attaining the lowest δ^{18}O values (-11.5 ‰) of the entire record, suggesting the strongest

269   pluvial event (Duan P et al., 2023). This overshoot is additionally supported by trace element ratio record which show

270   quite low values relative to the period before 8.52 ka BP. However, the rebound of the δ^{13}C during the post-8.2 ka

271   event is not as conspicuous as the δ^{18}O overshoot and only reaches the mean level of that preceding the 8.5 ka event.

272   These features further illustrate the aforementioned nonlinear relationship among the variabilities of regional climate,

273   local hydrological condition, and ecosystem. In other words, the coverage of vegetation and soil microbiological

274   activity during the overshoot event didn't recover to the initial conditions before the 8.2 ka event.

275   The different behavior of δ^{13}C after two similar severe droughts at 8.50 and 8.20 ka BP suggests the degree of resilient

276   ecosystem to the different rebound rainfall intensity. For the 8.5 ka event, the subsequent rebound of δ^{13}C to its prior

277   value suggests the high-level resilience of the plant community to environmental variations under the moderate

278   precipitation amount as indicated by the δ^{18}O and trace element ratio records. In contrast, the suddenly excessive

279   increase of precipitation after the 8.2 ka event, which was much more than that before the event, could have suppressed

280   the recovery of vegetation and soil biological activity and thus the moderate rebound of $\delta^{13}C$ values. Theoretically,

281   the longer weakened atmospheric circulation during the 8.2 ka event and reduced precipitation presumably induced

282   deteriorated vegetation as well as poor-developed soil. However, it seems that the precipitation intensity after the 8.2

283   ka event exerted a key role on the recovery of vegetation density and soil productivity. Specifically, the severe 8.2 ka

284   drought event had a profoundly negative impact on the vegetation-soil system and led them to become more vulnerable

285   under the water shortage conditions. On the other hand, the excessive precipitation after this drought could cause soil

286   erosion and further ecological damage, suppressing the ecosystem recovery above the cave as well as the $\delta^{13}C$ signals

287   in speleothem. Conclusively, the ecosystem in this karst region was quite vulnerable and the variability of the

288   vegetation-soil system here was tied to local hydrologic conditions with both high and low thresholds.

289   To summarize, akin to the $\delta^{18}O$ record, other proxy records of the BH-2 (Figure 2) delineate two major drought events,

290   indicated by prominent excursions centered at 8.50 and 8.20 ka BP, respectively, suggesting vegetation degeneration

291   (Duan et al., 2014) and elevated prior calcite precipitation (PCP) arising from longer residence time of solution in the

292   karst aquifer (e.g., Johnson et al., 2006; Fairchild et al., 2009), both of which responded to the deteriorated

293   hydroclimatic conditions. The discrepancy between them could suggest that other drivers than only hydroclimatic

294   conditions possibly have played a non-negligible role in the processes of speleothem formation. In particular, the

295   intensity of the EASM ($\delta^{18}O$) and the precipitation amount (trace element ratio) over the study area presumably were

296   definitely correlated on a broad pattern but did not necessarily exactly follow each other.

297   **4.3 Spatial patterns for the two drought-one pluvial pattern and underlying mechanisms**

298   This two drought-one pluvial pattern from 8.52 to 8.0 ka BP in speleothem BH-2 represents global scale climate

299   disturbance signals rather than a regional phenomenon since these climate excursions have been widely documented

300   (Figures 3 and S1). In the ASM domain, speleothem records from such as Lianhua (Dong et al., 2018), Wuya (Tan et

301   al., 2020) Caves in North and Northwest China, and Qingtian Cave (Liu et al., 2015) in central China exhibit consistent

302   structure with the BH-2 at around 8.2 ka BP. In particular, a broad anomaly spanning ~340 years between 8.46 and

303   8.12 ka BP has been revealed (Tan et al., 2020) and we find the post-8.2 ka overshoot is also distinguishable (Figure

304   3) in the speleothem $\delta^{18}O$ record from the western Chinese Loess Plateau which is situated in the northern limit of the

305   ASM. Unlike these north-located records, although a prominent 8.2 ka event is documented in speleothem of Heshang

306   Cave in central China (Liu et al., 2013), the preceded excursion is ambiguous and the post-8.2 ka event anomaly is

307   absent. Coincidently, a similar phenomenon seems to occur in the central monsoon domain, like Dongge Cave in

308   South China (Cheng et al., 2009) and Tham Doun Mai Cave from northern Laos (Wood et al., 2023). This probably

309   suggests that, compared to the low latitudes, the climate in the north part (or the margin area) of the ASM is more

310   sensitive to the climate perturbation signals originating from the high northern latitude regions. Through affecting the

311   westerly changes, high northern latitude climate variations can finally strongly influence the EASM (Chiang et al.,

312   2015; Duan et al., 2016; Tan et al., 2020).

313   In the low latitudes of the Indian summer monsoon realm, the speleothem $\delta^{18}O$ record from Hoti Cave is remarkably

314   consistent with the pattern in our record. Specifically, Hoti Cave record shows positive $\delta^{18}O$ excursions by ~2 ‰ in

315   amplitude centering ~8.42 ka BP and a growth hiatus at 8.2 ka BP surrounded by enriched ^{18}O, pointing to the drought

316 conditions due to the weakened Indian summer monsoon attendant with a southward shift of the intertropical
317 convergence zone (ITCZ). After the growth resumption, an overshoot can be identified (Cheng et al., 2009). It happens
318 that the two positive excursions are quite pronounced in nearby Qunf Cave (Figure 3) (Cheng et al., 2009), whereas
319 the overshoot is absent. Collectively, records from more sensitive areas in the ASM domain intactly preserved the two
320 drought-one pluvial pattern, while the pre-8.2 ka event or the overshoot is missed in records from insensitive regions.
321 In the North Atlantic region, Greenland ice core $\delta^{18}O$ (Thomas et al., 2007) and reconstructed temperature based on
322 argon and nitrogen isotopes (Kobashi et al., 2017) captured both the 8.2 ka event and ensuing overshoot, and the pre-
323 8.2 ka event is apparent in the temperature profile but ambiguous or slightly excursed (Jennings et al., 2015) in the
324 $\delta^{18}O$ records. Indeed, the atmospheric circulation over Greenland has substantially changed since ~8.5 ka BP as
325 suggested by increased potassium and calcium ions, indicators of dust supply to Greenland, as well as decreased snow-
326 accumulation rate (Rohling and Pälike, 2005; Kobashi et al., 2017; Burstyn et al., 2019). The absent signal of the pre-
327 8.2 ka event in $\delta^{18}O$ records could be attributed to the compensation of other processes like precipitation seasonality
328 and summer warming (He et al., 2021). The prolonged climate anomalies around 8.2 ka BP are further supported by
329 two negative anomalies in speleothem $\delta^{18}O$ records from Italy (Domínguez-Villar et al., 2009) and Hungary (Demény
330 et al., 2023), lower tree ring width from 8.42 to 8.0 ka BP in Germany (Spurk et al., 2002), as well as degraded climate
331 conditions between 8.45 and 8.10 ka BP revealed by speleothem proxies from Père Noël Cave in Belgium (Allan et
332 al., 2017). All of these collectively suggest a series of pronounced climate oscillations between 8.5 and 8.0 ka BP,
333 instead of merely the 8.2 ka event, is of hemispheric significance (Rohling and Pälike, 2005). In the North America,
334 multi-proxy speleothem records manifest more sustained increase in precipitation in both precursor and 8.2 ka event
335 responding to the increased North Pacific storm in California (de Wet et al., 2021).
336 Similar but antiphase patterns are observed in the records from the Southern Hemisphere. For example, it appears that
337 speleothem record from Lapa Grand Cave in East Brazil (Stríkis et al., 2011) captured the two pluvial-one drought
338 structure (Figure 3). Intriguingly, although speleothem record from Padre Cave (Cheng et al., 2009) fails to preserve
339 a remarkable pre-8.2 ka event (Figure 3), two negative short excursions and a seemingly negative trend can be
340 observed from 8.34 to 8.23 ka BP. Besides, the beginning deposit of speleothem in Padre Cave at ~8.5 ka BP, coeval
341 with the reduced precipitation in the ASM domain, likely reflects more favorable hydroclimatic conditions due to
342 more precipitation, which in turn could arise from intensified South American summer monsoon associated with the
343 southward displacement of the ITCZ (Wang X et al., 2004), suggesting the possible occurrence of the pre-8.2 ka event
344 there. Coincidentally, the speleothem growth resumption after a long hiatus (Duan P et al., 2021), together with the
345 negative trend of speleothem $\delta^{18}O$ record (Voarintsoa et al., 2019) in Northwest Madagascar commenced at ~8.5 ka
346 BP and persisted until the end of the 8.2 ka event, indicative of more precipitation in response to the southward ITCZ
347 shift, suggesting the extent of the pre-8.2 ka event to the East Africa monsoon domain. However, the post-8.2 ka event
348 was not clearly identified by the Northwest Madagascar record and thus more evidence is needed.
349 The two droughts-one pluvial pattern revealed in our BH-2 records could mainly correspond to the waxing and waning
350 of drainages of the lakes Agassiz and Ojibway (LAO) (Barber et al., 1999; Ellison et al., 2006) and contemporary ice
351 sheet melted freshwater flux (Matero et al., 2017, 2020) (Figure 3), both of which causally related to the AMOC
352 strength dynamics. Firstly, the major two-step outburst of the LAO (e.g., Ellison et al., 2006; Kleiven et al., 2008;

353 Jennings et al., 2015; Lochte et al., 2018; Godbout et al., 2019, 2020) and the continuous Laurentide Ice Sheet (LIS)

354 melting together contributed to the increase of total freshwater flux (e.g., Morrill et al., 2014; Matero et al., 2017,

355 2020), inducing observed sea level rise in North Atlantic commencing ~8.5 ka BP (Hijma et al., 2010), cooling

356 conditions initially in the circum-North Atlantic region and perturbed into other areas through fast atmospheric

357 propagations (Cheng et al., 2009, 2020; Liu et al., 2013; Buizert et al., 2014; Duan P et al., 2021). Coincident with

358 enriched $^{18}O_p$ in most ASM domains, the intensity of the East Asian summer monsoon was weakened (Cheng et al.,

359 2009) and less precipitation fell in the Beijing area (Duan P et al., 2023). In contrast, due to the southward displacement

360 of the ITCZ in response to the hemispheric thermal contrast, the Southern Hemisphere, like Northeast Madagascar

361 and East Brazil, received more precipitation (i.e., stronger monsoon) and thus speleothem records there exhibit

362 depleted $^{18}O_p$. Further, the simulated smaller freshwater flux peak at ~8.5 ka BP relative to the second one at 8.2 ka

363 (Figure 3) (Matero et al., 2020) could provide a potential explanation for the lower amplitude and shorter duration of

364 the pre-8.2 ka event relative to the 8.2 ka event in our record and the absence of the pre-8.2 ka event in other records.

365 Additionally, the 8.2 ka event is preceded by a remarkable reduction in solar activity by ~1 Wm^{-2} with a duration of

366 ~150 years, beginning at ~8.45 ka BP (Rohling and Pälike, 2005; Steinhilber et al., 2009; Wanner et al., 2011; Burstyn

367 et al., 2019), and an increase in the magnitude and frequency of volcanic eruptions (Kobashi et al., 2017; Burstyn et

368 al., 2019), both of which are also thought to contribute to the prolonged climate disturbance via different impacts on

369 atmospheric processes.

370 On the other hand, the overshoot in the ASM domain could be remotely related to the higher temperature in the North

371 Atlantic (Kobashi et al., 2017; Andersen et al., 2017) (Figure 3) which in turn possibly arose from the remarkably

372 speed-up AMOC (Ellison et al., 2006; Renold et al., 2010; Mjell et al., 2015; Andersen et al., 2017). The accelerated

373 AMOC led to more heat release in the North Atlantic and anomalously strengthened ASM. In the meanwhile, the

374 ITCZ and associated rainbelt were displaced northwards, causing less precipitation in east Brazil as evidenced by

375 positive $\delta^{18}O$ excursion of speleothem from Lapa Grande Cave (Figure 3).

376 **5 Conclusions**

377 The multi-proxy records of speleothem BH-2 from Beijing, North China document the multi-decadal to centennial

378 scale hydroclimate changes with two arid episodes at ~8.5 and 8.2 ka BP, and an immediately ensuing excessive

379 rebound after the 8.2 ka event. A comparison with other paleoclimate records suggests that these prominent climate

380 fluctuations with two drought-one pluvial pattern should be a global signal instead of a regional phenomenon. We

381 propose that the slowdown and resumption of the AMOC controlled by the freshwater flux into the North Atlantic and

382 the resultant reorganization of the atmospheric circulation during the study stage mainly contribute to the arid and

383 pluvial excursions, and the influence of volcanic outbursts and reduced solar activity are also non-negligible.

384 **Data availability**

385 All data needed to evaluate the conclusions in the paper are presented in the paper. The data will be archived at the

386 NOAA National Climate Data Center (https://www.ncdc.noaa.gov/data-access/paleoclimatology-data) when this

387 manuscript is accepted.

Author contributions

PD, HL and HC designed the research and experiments. PD wrote the first draft of the paper. HL, HC, and AS revised the manuscript. ZM did the fieldwork and collected the samples. ZM and HC conducted the [230]Th dating. ZM, HC, and PD conducted the oxygen isotope measurements. All authors discussed the results and provided inputs on the manuscript.

Competing interests

The authors declare that they have no conflict of interest.

Acknowledgments

This work was supported by the National Natural Science Foundation of China grants (No. 41888101 and 42150710534 to H.C., 42230812 to G.Z., and 42102229 to H.L.) and China Postdoctoral Science Foundation (No. 2021M692522). We specially thank Ming Tan and Wuhui Duan from Institute of Geology and Geophysics, Chinese Academy of Sciences for their helpful suggestions. We also thank Haibo Wang, Lijuan Sha and Jiayu Lu for their help on the sample measurements and data curation.

References

Aguiar, W., Meissner, K. J., Montenegro, A., Prado, L., Wainer, I., and Carlson, A. E.: Magnitude of the 8.2 ka event freshwater forcing based on stable isotope modelling and comparison to future Greenland melting, Sci. Rep., 11, 1–10, https://doi.org/10.1038/s41598-021-84709-5, 2021.

Allan, M., Fagel, N., van der Lubbe, H. J. L., Vonhof, H. B., Cheng, H., Edwards, R. L., and Verheyden, S.: High-resolution reconstruction of 8.2-ka BP event documented in Père Noël cave, southern Belgium, J. Quat. Sci., 33, 840–852, https://doi.org/10.1002/jqs.3064, 2018.

Alley, R. B., Mayewski, P. A., Sowers, T., Stuiver, M., Taylor, K. C., and Clark, P. U.: Holocene climatic instability: a prominent, widespread event 8200 yr ago, Geology, 25, 483–486, https://doi.org/10.1130/0091-7613(1997)025<0483: HCIAPW>2.3.CO;2, 1997.

Andersen, N., Lauterbach, S., Erlenkeuser, H., Danielopol, D. L., Namiotko, T., and Hüls, M.: Evidence for higher-than-average air temperatures after the 8.2 ka event provided by a Central European $\delta^{18}O$ record, Quat. Sci. Rev., 172, 96–108, http://dx.doi.org/10.1016/j.quascirev.2017.08.001, 2017.

Banner, J. L., Guilfoyle, A., James, E. W., Stern, L. A., and Musgrove, M.: Seasonal variations in modern speleothem calcite growth in central Texas, USA, J. Sediment. Res., 77, 615–622, https://doi.org/10.2110/jsr.2007.065, 2007.

Barber, D. C., Dyke, A., Hillaire-Marcel, C., Jennings, A. E., Andrews, J. T., and Kerwin, M. W.: Forcing of the cold event of 8,200 years ago by catastrophic drainage of Laurentide lakes, Nature, 400, 344, https://doi.org/10.1038/22504, 1999.

419 Baker, A., Asrat, A., Fairchild, I. J., Leng, M. J., Wynn, P. M., Bryant, C., Genty, D., and Umer, M.: Analysis of the

420 climate signal contained within $\delta^{18}O$ and growth rate parameters in two Ethiopian stalagmites, Geochim. Cosmochim.

421 Acta., 71, 2975–2988, https://doi.org/10.1016/j.gca.2007.03.029, 2007.

422 Buizert, C., Sigl, M., Severi, M., Markle, B. R., Wettstein, J. J., and McConnell, J. R.: Abrupt ice-age shifts in southern

423 westerly winds and Antarctic climate forced from the north, Nature, 563, 681–685, https://doi.org/10.1038/s41586-

424 018-0727-5, 2018.

425 Burstyn, Y., Martrat, B., Lopez, J. F., Iriarte, E., Jacobson, M. J., Lone, M. A., and Deininger, M.: Speleothems from

426 the Middle East: an example of water limited environments in the SISAL database, Quaternary, 2, 16,

427 https://doi.org/10.3390/quat2020016, 2019.

428 Cheng, H., Edwards, R. L., Shen, C. C., Polyak, V. J., Asmerom, Y., and Woodhead, J.: Improvements in ^{230}Th dating,

429 ^{230}Th and ^{234}U half-life values, and U-Th isotopic measurements by multi-collector inductively coupled plasma mass

430 spectrometry, Earth. Planet. Sci. Lett., 371–372, 82–91, https://doi.org/10.1016/j.epsl.2013.04.006, 2013.

431 Cheng, H., Fleitmann, D., Edwards, R. L., Wang, X., Cruz, F. W., and Auler, A. S.: Timing and structure of the 8.2

432 kyr B.P. event inferred from $\delta^{18}O$ records of stalagmites from China, Oman, and Brazil, Geology, 37, 1007–1010,

433 https://doi.org/10.1130/G30126A.1, 2009.

434 Cheng, H., Li, H., Sha, L., Sinha, A., Shi, Z., Yin, Q., Lu, Z., Zhao, D., Cai, Y., Hu, Y., Hao, Q., Tian, J., Kathayat,

435 G., Dong, X., Zhao, J., and Zhang, H.: Milankovitch theory and monsoon, Innovation, 3, 100338,

436 https://doi.org/10.1016/j. xinn.2022.100338, 2022.

437 Cheng, H., Zhang, H., Spotl, C., Baker, J., Sinha, A., and Li, H.: Timing and structure of the Younger Dryas event

438 and its underlying climate dynamics, Proc. Natl. Acad. Sci. USA., 117, 23408–23417,

439 https://doi.org/10.1073/pnas.2007869117, 2020.

440 Cheng, H., Zhang, H., Cai, Y., Shi, Z., Yi, L., Deng, C., and Perez-Mejías, C.: Orbital-scale Asian summer monsoon

441 variations: Paradox and exploration, Sci. China. Earth. Sci., 64, 529–544, https://doi.org/10.1007/s11430-020-9720-

442 y, 2021.

443 Chiang, J. C., Fung, I. Y., Wu, C. H., Cai, Y., Edman, J. P., Liu, Y., and Labrousse, C. A.: Role of seasonal transitions

444 and westerly jets in East Asian paleoclimate. Quat. Sci. Rev., 108, 111–129,

445 https://doi.org/10.1016/j.quascirev.2014.11.009, 2015.

446 Cruz, F., Burns, S., Jercinovic, M., Karmann, I., Sharp, W., and Vuille, M.: Evidence of rainfall variations in Southern

447 Brazil from trace element ratios (Mg/Ca and Sr/Ca) in a Late Pleistocene stalagmite, Geochem. Cosmochim. Acta.,

448 71, 2250–2263, https://doi.org/10.1016/j.gca.2007.02.005, 2007.

449 Daley, T. J., Street-Perrott, F. A., Loader, N. J., Barber, K. E., Hughes, P. D., Fisher, E. H., and Marshall, J. D.:

450 Terrestrial climate signal of the "8200 yr BP cold event" in the Labrador Sea region, Geology, 37, 831–834,

451 https://doi.org/10.1130/G30043A.1, 2009.

452 Domínguez-Villar, D., Fairchild, I. J., Baker, A., Wang, X., Edwards, R. L., and Cheng, H.: Oxygen isotope

453 precipitation anomaly in the North Atlantic region during the 8.2 ka event, Geology, 37, 1095–1098,

454 https://doi.org/10.1130/G30393A.1, 2009.

Dong, J., Shen, C. C., Kong, X., Wu, C. C., Hu, H. M., Ren, H., and Wang, Y.: Rapid retreat of the East Asian summer monsoon in the middle Holocene and a millennial weak monsoon interval at 9 ka in northern China, J. Asian. Earth. Sci., 151, 31–39, https://doi.org/10.1016/j.jseaes.2017.10.016, 2018.

Dorale, J. A., and Liu, Z.: Limitations of Hendy test criteria in judging the paleoclimatic suitability of speleothems and the need for replication, J. Caves. Karst. Stud., 71, 73–80, 2009.

Duan, P., Li, H., Sinha, A., Voarintsoa, N. R. G., Kathayat, G., Hu, P., and Cheng, H.: The timing and structure of the 8.2 ka event revealed through high-resolution speleothem records from northwestern Madagascar, Quat. Sci. Rev., 268, 107104, https://doi.org/10.1016/j.quascirev.2021.107104, 2021.

Duan, P., Li, H., Ma, Z., Zhao, J., Dong, X., Sinha, A., and Cheng, H.: Interdecadal to centennial climate variability surrounding the 8.2 ka event in North China revealed through an annually resolved speleothem record from Beijing, Geophys. Res. Lett., 50, e2022GL101182, https://doi.org/10.1029/2022GL101182, 2023.

Duan, W., Ma, Z., Tan, M., Cheng, H., Edwards, R. L., and Wen, X.: Timing and structure of early-Holocene climate anomalies inferred from north Chinese stalagmite records, Holocene, 31, 1777–1785, https://doi.org/10.1177/09596836211033218, 2021.

Duan, W., Ruan, J., Luo, W., Li, T., Tian, L., and Zeng, G.: The transfer of seasonal isotopic variability between precipitation and drip water at eight caves in the monsoon regions of China, Geochim. Cosmochim. Acta., 183, 250–266, http://dx.doi.org/10.1016/j.gca.2016.03.037, 2016.

Duan, W., Tan, M., Ma, Z., and Cheng, H.: The palaeoenvironmental significance of $\delta^{13}C$ of stalagmite BH-1 from Beijing, China during Younger Dryas intervals inferred from the grey level profile, Boreas, 43, 243–250, https://doi.org/10.1111/bor.12034, 2014.

Edwards, R. L., Chen, J. H., and Wasserburg, G. J.: ^{238}U-^{234}U-^{230}Th-^{232}Th systematics and the precise measurement of time over the past 500,000 years, Earth Planet. Sci. Lett., 81, 175–192, https://doi.org/10.1016/0012-821X(87)90154-3, 1987.

Ellison, C. R., Chapman, M. R., and Hall, I. R.: Surface and deep ocean interactions during the cold climate event 8200 years ago, Science, 312, 1929–1932, https://doi.org/10.1126/science.1127213, 2006.

Fairchild, I. J., Borsato, A., Tooth, A. F., Frisia, S., Hawkesworth, C. J., Huang, Y., and Spiro, B.: Controls on trace element (Sr-Mg) compositions of carbonate cave waters: implications for speleothem climatic records, Chem. Geol., 166, 255–269, https://doi.org/10.1016/S0009-2541(99)00216-8, 2000.

Fairchild, I. J., Smith, C. L., Baker, A., Fuller, L., Spötl, C., Mattey, D., Chem. Geol., and McDermott, F.: Modification and preservation of environmental signals in speleothems, Earth. Sci. Rev., 75, 105–153, https://doi.org/10.1016/j.earscirev.2005.08.003, 2006.

Fairchild, I. J., Chem. Geol., and Treble, P. C.: Trace elements in speleothems as recorders of environmental change, Quat. Sci. Rev., 449–468, https://doi.org/10.1016/j.quascirev.2008.11.007, 2009.

Fleitmann, D., Burns, S. J., Mudelsee, M., Neff, U., Kramers, J., Mangini, A., and Matter, A.: Holocene forcing of the Indian monsoon recorded in a stalagmite from southern Oman, Science, 300, 1737–1739, https://doi.org/10.1126/science.1083130, 2003.

491 Fohlmeister, J.: A statistical approach to construct composite climate records of dated archives, Quat. Geochronol.,

492 14, 48–56, https://doi.org/10.1016/j.quageo.2012.06.007, 2012.

493 Gauthier, M. S., Kelley, S. E., and Hodder, T. J.: Lake Agassiz drainage bracketed Holocene Hudson Bay ice saddle

494 collapse, Earth Planet. Sci. Lett., 544, 116372, https://doi.org/10.1016/j.epsl.2020.116372, 2020.

495 Godbout, P. M., Roy, M., and Veillette, J. J.: High-resolution varve sequences record one major late-glacial ice

496 readvance and two drainage events in the eastern Lake Agassiz-Ojibway basin, Quat. Sci. Rev., 223, 105942,

497 https://doi.org/10.1016/j.quascirev.2019.105942, 2019.

498 Godbout, P. M., Roy, M., and Veillette, J. J.: A detailed lake-level reconstruction shows evidence for two abrupt lake

499 drawdowns in the late-stage history of the eastern Lake Agassiz-Ojibway basin, Quat. Sci. Rev., 238, 106327,

500 https://doi.org/10.1016/j.quascirev.2020.106327, 2020.

501 Griffiths, M., Drysdale, R., Gagan, M., Frisia, S., Zhao, J., Ayliffe, L., Hantoro, W., Hellstrom, J., Fischer, M., and

502 Feng, Y.: Evidence for Holocene changes in Australian-Indonesian monsoon rainfall from stalagmite trace element

503 and stable isotope ratios, Earth Planet. Sci. Lett., 292, 27–38, https://doi.org/10.1016/j.epsl.2010.01.002, 2010.

504 He, C., Liu, Z., Otto-Bliesner, B. L., Brady, E. C., Zhu, C., Tomas, R., and Bao, Y.: Hydroclimate footprint of pan-

505 Asian monsoon water isotope during the last deglaciation, Sci. Adv., 7, eabe2611,

506 https://doi.org/10.1126/sciadv.abe2611, 2021.

507 Hersbach, H., Bell, B., Berrisford, P., Hirahara, S., Horányi, A., and Muñoz-Sabater, J.: The ERA5 global reanalysis,

508 Q. J. R .Meteorol. Soc., 146, 1999–2049, https://doi.org/10.1002/qj.3803, 2020.

509 Hijma, M. P., and Cohen, K. M.: Timing and magnitude of the sea-level jump preluding the 8200 yr event, Geology,

510 38, 275–278, https://doi.org/10.1130/G30439.1, 2010.

511 Hughen, K. A., Overpeck, J. T., Peterson, L. C., and Trumbore, S.: Rapid climate changes in the tropical Atlantic

512 region during the last deglaciation, Nature, 380, 51–54, https://doi.org/10.1038/380051a0, 1996.

513 Jansson, K. N., and Kleman, J.: Early Holocene glacial lake meltwater injections into the Labrador Sea and Ungava

514 Bay, Paleoceanography, 19, PA1001, https://doi.org/10.1029/2003PA000943, 2004.

515 Jennings, A., Andrews, J., Pearce, C., Wilson, L., and Ólfasdótttir, S.: Detrital carbonate peaks on the Labrador shelf,

516 a 13–7 ka template for freshwater forcing from the Hudson Strait outlet of the Laurentide Ice Sheet into the subpolar

517 gyre, Quat. Sci. Rev., 107, 62–80, https://doi.org/10.1016/j.quascirev.2014.10.022, 2015.

518 Johnson, K. R., Hu, C., Belshaw, N. S., and Henderson, G. M.: Seasonal trace-element and stable-isotope variations

519 in a Chinese speleothem: The potential for high-resolution paleomonsoon reconstruction, Earth Planet. Sci. Lett., 244,

520 394–407, https://doi.org/10.1016/j.epsl.2006.01.064, 2006.

521 Kerwin, M. W.: A regional stratigraphic isochron (ca. 8000 ^{14}C yr BP) from final deglaciation of Hudson Strait, Quat

522 Res., 46, 89–98, https://doi.org/10.1006/qres.1996.0049, 1996.

523 Kleiven, H. K. F., Kissel, C., Laj, C., Ninnemann, U. S., Richter, T. O., and Cortijo, E.: Reduced North Atlantic deep

524 water coeval with the glacial Lake Agassiz freshwater outburst, Science, 319, 60–64,

525 https://doi.org/10.1126/science.1148924, 2008.

526 Kobashi, T., Menviel, L., Jeltsch-Thömmes, A., Vinther, B. M., Box, J. E., and Muscheler, R.: Volcanic influence on

527 centennial to millennial Holocene Greenland temperature change, Sci. Rep., 7, 1–10, https://doi.org/10.1038/s41598-

528 017-01451-7, 2017.

529 Kobashi, T., Severinghaus, J. P., Brook, E. J., Barnola, J.-M., and Grachev, A. M.: Precise timing and characterization

530 of abrupt climate change 8200 years ago from air trapped in polar ice, Quat. Sci. Rev., 26, 1212–1222,

531 https://doi.org/10.1016/j.quascirev.2007.01.009, 2007.

532 Krklec, K., and Dominguez-Villar, D.: Quantification of the impact of moisture source regions on the oxygen isotope

533 composition of precipitation over Eagle Cave, central Spain, Geochim. Cosmochim. Acta., 134, 39–54,

534 https://doi.org/10.1016/j.gca.2014.03.011, 2014.

535 Lajeunesse, P., and St-Onge, G.: The subglacial origin of the Lake Agassiz-Ojibway final outburst flood, Nat. Geosci.,

536 1, 184–188, https://doi.org/10.1038/ngeo130, 2008.

537 Lawrence, T., Long, A. J., Gehrels, W. R., Jackson, L. P., and Smith, D. E.: Relative sea-level data from southwest

538 Scotland constrain meltwater-driven sea-level jumps prior to the 8.2 kyr BP event, Quat. Sci. Rev., 151, 292–308,

539 https://doi.org/10.1016/j.quascirev.2016.06.013, 2016.

540 LeGrande, A. N., and Schmidt, G. A.: Ensemble, water isotope-enabled, coupled general circulation modeling insights

541 into the 8.2 ka event, Paleoceanography, 23, PA3207, https://doi.org/10.1029/2008PA001610, 2008.

542 Li, H., Cheng, H., and Wang, J.: Applications of laser induced breakdown spectroscopy to paleoclimate research:

543 reconsturcting speleothem trace element records, Quat Sci., 38, 1549–1551 (in Chinese), 2018.

544 Li, H., Sinha, A., Anquetil André, A., Spötl, C., Vonhof, H. B., Meunier, A., and Cheng, H.: A multimillennial climatic

545 context for the megafaunal extinctions in Madagascar and Mascarene Islands, Sci. Adv., 6, eabb2459,

546 https://doi.org/10.1126/sciadv.abb2459, 2020.

547 Li, X., Cheng, H., Tan, L., Ban, F., Sinha, A., and Duan, W.: The East Asian summer monsoon variability over the

548 last 145 years inferred from the Shihua Cave record, North China, Sci. Rep., 7, 7078, https://doi.org/10.1038/s41598-

549 017-07251-3, 2017.

550 Li, Y., Rao, Z., Xu, Q., Zhang, S., Liu, X., Wang, Z., and Chen, F.: Inter-relationship and environmental significance

551 of stalagmite $\delta^{13}C$ and $\delta^{18}O$ records from Zhenzhu Cave, north China, over the last 130 ka, Earth Planet. Sci. Lett.,

552 536, 116149, https://doi.org/10.1016/j.epsl.2020.116149, 2020.

553 Liu, D., Wang, Y., Cheng, H., Edwards, R. L., and Kong, X.: Cyclic changes of Asian monsoon intensity during the

554 early mid-Holocene from annually-laminated stalagmites, central China, Quat. Sci. Rev., 121, 1–10,

555 https://doi.org/10.1016/j.quascirev.2015.05.003, 2015.

556 Liu, Y., Henderson, G. M., Hu, C., Mason, A. J., Charnley, N., and Johnson, K. R.: Links between the East Asian

557 monsoon and north Atlantic climate during the 8,200 year event, Nat. Geosci., 6, 117–120,

558 https://doi.org/10.1038/ngeo1708, 2013.

559 Liu, Z., Wen, X., Brady, E. C., Otto-Bliesner, B., Yu, G., Lu, H., and Yang, H.: Chinese cave records and the East

560 Asia summer monsoon, Quat. Sci. Rev., 83, 115–128, https://doi.org/10.1016/j.quascirev.2013.10.021, 2014.

561 Lochte, A. A., Repschläger, J., Kienast, M., Garbe-Schönberg, D., Andersen, N., and Hamann, C.: Labrador Sea

562 freshening at 8.5 ka BP caused by Hudson Bay Ice Saddle collapse, Nat. Commun., 10, 1–9,

563 https://doi.org/10.1038/s41467-019-08408-6, 2019.

564 Ma, Z., Cheng, H., Tan, M., Edwards, R. L., Li, H., and You, C.: Timing and structure of the Younger Dryas event in

565 northern China, Quat. Sci. Rev., 41, 83–93, https://doi.org/10.1016/j.quascirev.2012.03.006, 2012.

566 Matero, I. S. O., Gregoire, L. J., Ivanovic, R. F., Tindall, J. C., and Haywood, A. M.: The 8.2 ka cooling event caused

567 by Laurentide ice saddle collapse, Earth Planet. Sci. Lett., 473, 205–214, https://doi.org/10.1016/j.epsl.2017.06.011,

568 2017.

569 Matero, I. S., Gregoire, L. J., and Ivanovic, R. F.: Simulating the Early Holocene demise of the Laurentide Ice Sheet

570 with BISICLES (public trunk revision 3298), Geosci. Model. Dev., 13, 4555–4577, https://doi.org/10.5194/gmd-13-

571 4555-2020, 2020.

572 McDermott, F.: Palaeo-climate reconstruction from stable isotope variations in speleothems: a review, Quat. Sci. Rev.,

573 23, 901–918, https://doi.org/10.1016/j.quascirev.2003.06.021, 2004.

574 Mjell, T. L., Ninnemann, U. S., Eldevik, T., and Kleiven, H. K. F.: Holocene multidecadal-to millennial-scale

575 variations in Iceland-Scotland overflow and their relationship to climate, Paleoceanography, 30, 558–569,

576 https://doi.org/10.1002/2014PA002737, 2015.

577 Morrill, C., Anderson, D. M., Bauer, B. A., Buckner, R., Gille, E. P., Gross, W. S., Hartman, M., and Shah, A.: Proxy

578 benchmarks for intercomparison of 8.2 ka simulations, Clim. Past., 9, 423–432, https://doi.org/10.5194/cp-9-423-2013,

579 2013.

580 Morrill, C., Ward, E. M., Wagner, A. J., Otto-Bliesner, B. L., and Rosenbloom, N.: Large sensitivity to freshwater

581 forcing location in 8.2 ka simulations., Paleoceanography, 29, 930–945, https://doi.org/10.1002/2014PA002669, 2014.

582 Peros, M., Collins, S., G'Meiner, A. A., Reinhardt, E., and Pupo, F. M.: Multistage 8.2 kyr event revealed through

583 high-resolution XRF core scanning of Cuban sinkhole sediments, Geophys. Res. Lett., 44, 7374–7381,

584 https://doi.org/10.1002/2017GL074369, 2017.

585 Polyak, V. J., Rasmussen, J. B., and Asmerom, Y.: Prolonged wet period in the southwestern United States through

586 the Younger Dryas, Geology, 32, 5–8, https://doi.org/10.1130/G19957.1, 2004.

587 Renold, M., Raible, C. C., Yoshimori, M., and Stocker, T. F.: Simulated resumption of the North Atlantic meridional

588 overturning circulation-slow basin-wide advection and abrupt local convection, Quat. Sci. Rev., 29, 101–112,

589 https://doi.org/10.1016/j.quascirev.2009.11.005, 2010.

590 Rohling, E. J., and Pälike, H.: Centennial-scale climate cooling with a sudden cold event around 8,200 years ago,

591 Nature, 434, 975–979, https://doi.org/10.1038/nature03421, 2005.

592 Roy, M., Dell'Oste, F., Veillette, J. J., De Vernal, A., Hélie, J. F., and Parent, M.: Insights on the events surrounding

593 the final drainage of Lake Ojibway based on James Bay stratigraphic sequences, Quat. Sci. Rev., 30, 682–692,

594 https://doi.org/10.1016/j.quascirev.2010.12.008, 2011.

595 Scholz, D., and Hoffmann, D. L.: StalAge-An algorithm designed for construction of speleothem age models. Quat

596 Geochronol, 6, 369–382, https://doi.org/10.1016/j.quageo.2011.02.002, 2011.

Sodemann, H., Schwierz, C., and Wernli, H.: Interannual variability of Greenland winter precipitation sources: Lagrangian moisture diagnostic and North Atlantic Oscillation influence, J. Geophys. Res. -Atmos., 113, D3107, https://doi.org/10.1029/2007JD008503, 2008.

Spurk, M., Leuschner, H. H., Baillie, M. G., Briffa, K. R., and Friedrich, M.: Depositional frequency of German subfossil oaks: climatically and non-climatically induced fluctuations in the Holocene, Holocene, 12, 707–715, 2002.

Stein, A. F., Draxler, R. R., Rolph, G. D., Stunder, B. J., Cohen, M. D., and Ngan, F.: NOAA's HYSPLIT atmospheric transport and dispersion modeling system, B. Am. Meteorol. Soc., 96, 2059–2077, https://doi.org/10.1175/BAMS-D-14-00110.1, 2015.

Steinhilber, F., Beer, J., and Fröhlich, C.: Total solar irradiance during the Holocene, Geophys. Res. Lett., 36, https://doi.org/10.1029/2009GL040142, 2009.

Stríkis, N. M., Cruz, F. W., Cheng, H., Karmann, I., Edwards, R. L., and Vuille, M.: Abrupt variations in South American monsoon rainfall during the Holocene based on a speleothem record from central-eastern Brazil, Geology, 39, 1075–1078, https://doi.org/10.1130/G32098.1, 2011.

Tan, L., Li, Y., Wang, X., Cai, Y., Lin, F., Cheng, H., Ma, L., Sinha, A., and Edwards, R. L.: Holocene monsoon change and abrupt events on the western Chinese Loess Plateau as revealed by accurately dated stalagmites, Geophys. Res. Lett., 47, e2020GL090273, https://doi.org/10.1029/2020GL090273, 2020.

Teller, J. T., Leverington, D. W., and Mann, J. D.: Freshwater outbursts to the oceans from glacial Lake Agassiz and their role in climate change during the last deglaciation, Quat. Sci. Rev., 21, 879–887, https://doi.org/10.1016/S0277-3791(01)00145-7, 2002.

Thomas, E. R., Wolff, E. W., Mulvaney, R., Steffensen, J. P., Johnsen, S. J., and Arrowsmith, C.: The 8.2 ka event from Greenland ice cores, Quat. Sci. Rev., 26, 70–81, https://doi.org/10.1016/j.quascirev.2006.07.017, 2007.

Törnqvist, T. E., and Hijma, M. P.: Links between early Holocene ice-sheet decay, sea-level rise and abrupt climate change, Nat. Geosci., 5, 601–606, https://doi.org/10.1038/ngeo1536, 2012.

Voarintsoa, N. R. G., Matero, I. S., Railsback, L. B., Gregoire, L. J., Tindall, J., Sime, L., and Razanatseheno, M. O. M.: Investigating the 8.2 ka event in northwestern Madagascar: Insight from data-model comparisons, Quat. Sci. Rev., 204, 172–186, https://doi.org/10.1016/j.quascirev.2018.11.030, 2019.

Von Grafenstein, U., Erlernkeuser, H., and Trimborn, P.: Oxygen and carbon isotopes in modern fresh-water ostracod valves: assessing vital offsets and autecological effects of interest for palaeoclimate studies, Palaeogeogr. Palaeoclimatol. Palaeoecol., 148, 133–152, https://doi.org/10.1016/S0031-0182(98)00180-1, 1999.

Wagner, A. J., Morrill, C., Otto-Bliesner, B. L., Rosenbloom, N., and Watkins, K. R.: Model support for forcing of the 8.2 ka event by meltwater from the Hudson Bay ice dome, Clim. Dyn., 41, 2855–2873, https://doi.org/10.1007/s00382-013-1706-z, 2013.

Wang, X., Auler, A. S., Edwards, R. L., Cheng, H., Cristalli, P. S., Smart, P. L., and Shen, C. C.: Wet periods in northeastern Brazil over the past 210 kyr linked to distant climate anomalies, Nature, 432, 740–743, https://doi.org/10.1038/nature03067, 2004.

Wanner, H., Solomina, O., Grosjean, M., Ritz, S. P., and Jetel, M.: Structure and origin of Holocene cold events, Quat. Sci. Rev., 30, 3109–3123, https://doi.org/10.1016/j.quascirev.2011.07.010, 2011.

634   Wong, C. I., Banner, J. L., and Musgrove, M.: Holocene climate variability in Texas, USA: An integration of existing

635   paleoclimate data and modeling with a new, high-resolution speleothem record, Quat. Sci. Rev., 127, 155–173,

636   https://doi.org/10.1016/j.quascirev.2015.06.023, 2015.

637   Wood, C. T., Johnson, K. R., Lewis, L. E., Wright, K., Wang, J. K., and Borsato, A.: High-resolution, multiproxy

638   speleothem record of the 8.2 ka event from Mainland Southeast Asia. Paleoceanogr Paleocl, 38, e2023PA004675.

639   https://doi.org/10.1029/2023PA004675, 2023.

640   Yoshimura, K., Kanamitsu, M., Noone, D., and Oki, T.: Historical isotope simulation using reanalysis atmospheric

641   data, J. Geophys. Res. -Atmos., 113, D19108, https://doi.org/10.1029/2008JD010074, 2008.

642   Zhang, H., Griffiths, M. L., Chiang, J. C., Kong, W., Wu, S., Atwood, A., and Xie, S.: East Asian hydroclimate

643   modulated by the position of the westerlies during Termination I, Science, 362, 580–583,

644   https://doi.org/10.1126/science.aat9393, 2018.

645   Zhao, J., Cheng, H., Cao, J., Sinha, A., Dong, X., Pan, L., Pérez-Mejías, C., Zhang, H., Li, H., Wang, J., Wang, K.,

646   Cui, J., and Yang, Y.: Orchestrated decline of Asian summer monsoon and Atlantic meridional overturning circulation

647   in global warming period, The Innovat. Geosci., 1, 100011, https://doi.org/10.59717/j.xinn- geo.2023.100011, 2023.

648
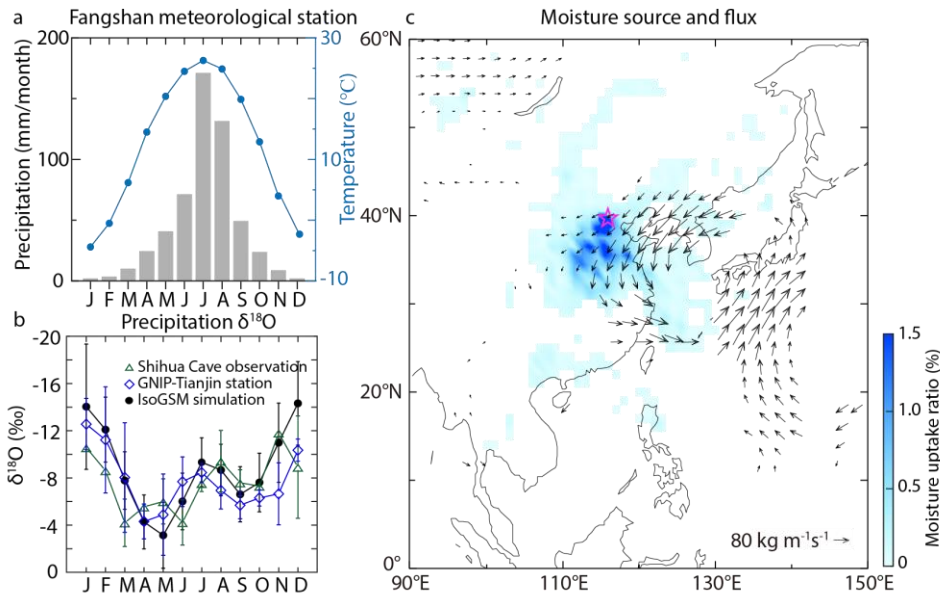
Figure 1. Climatology and locations. (**a**) Climographs of precipitation amount (gray bars) and temperature (blue dots connected with lines) at Fangshan Station (39°46′N, 116°28′E) near the study site, based on Chinese Meteorological Administration data (http://www.cma.gov.cn/). (**b**) Annual cycle comparison of $\delta^{18}O_p$ from observations of GNIP Tianjin station (https://www.iaea.org/services/networks/gnip) (1988–2002 CE with absent data covering 1993–2000 CE, blue triangles), Shihua Cave (Duan et al., 2016) (2011–2014 CE, green diamonds), and IsoGSM-simulation data (Yoshimura et al., 2008) (1979–2017 CE, black dots) at the Huangyuan Cave. Error bars represent the 1σ uncertainty of $\delta^{18}O_p$ values for each month. (**c**) Mean July-August (JA) moisture source region (blue shading) the Hybrid Single Particle Lagrangian Integrated Trajectory (HYSPLIT) model version 4.0 (Stein et al., 2015) based on the NOAA-NCEP/NCAR reanalysis global meteorological field data of 2010–2020 CE (Sodemann et al., 2008; Krklec and Dominguez-Villar, 2014) and water vapor flux (arrow) from the European Centre for Medium-Range Weather Forecasts Reanalysis fifth-generation dataset (ERA5) (Hersbach et al., 2020) between 1980 and 2015 CE.
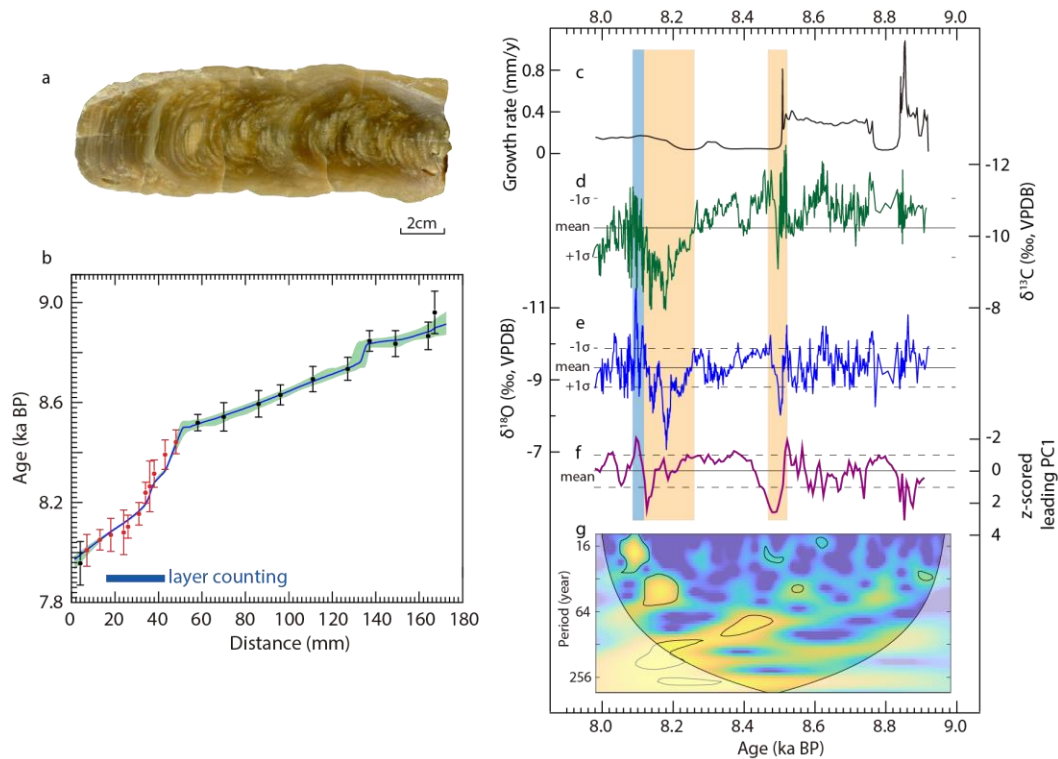
Figure 2. Age model and proxy profiles of speleothem BH-2. (**a**) Scanned image of speleothem BH-2. The scale of sample is similar with the x-axis of the subpanel **b**. (**b**) Stalage-derived age model (red, Scholz and Hoffmann, 2011) with 95 % confidence interval (light blue shading). Error bars on ^{230}Th dates represent 2σ analytical errors. The red dates indicate the published results of Duan et al. (2023). The horizontal blue bar marks the range with layer counting. (**c**) The inferred growth rate of the BH-2 based on the chronology in (**b**). (**d**) and (**e**) are δ^{18}O (dark blue) and δ^{13}C (green) profiles, respectively. The mean (solid) and the ±1σ values (dashed) for each entire record are indicated by the horizontal lines. (**f**) 30-year loess filtered *z*-scored leading PC1 record of trace element ratios of Ba/Ca, Mg/Ca, and Sr/Ca (see Figure S3). The mean value of the PC1 record is presented. (**g**) Wavelet periodicity analysis result of δ^{18}O. The 10% significance level against red noise is shown as a thick contour. The vertical yellow bars in the right subpanel mark the anomalously positive episodes and the light blue bar indicates the subsequent δ^{18}O overshoot after the 8.2 ka event.

672
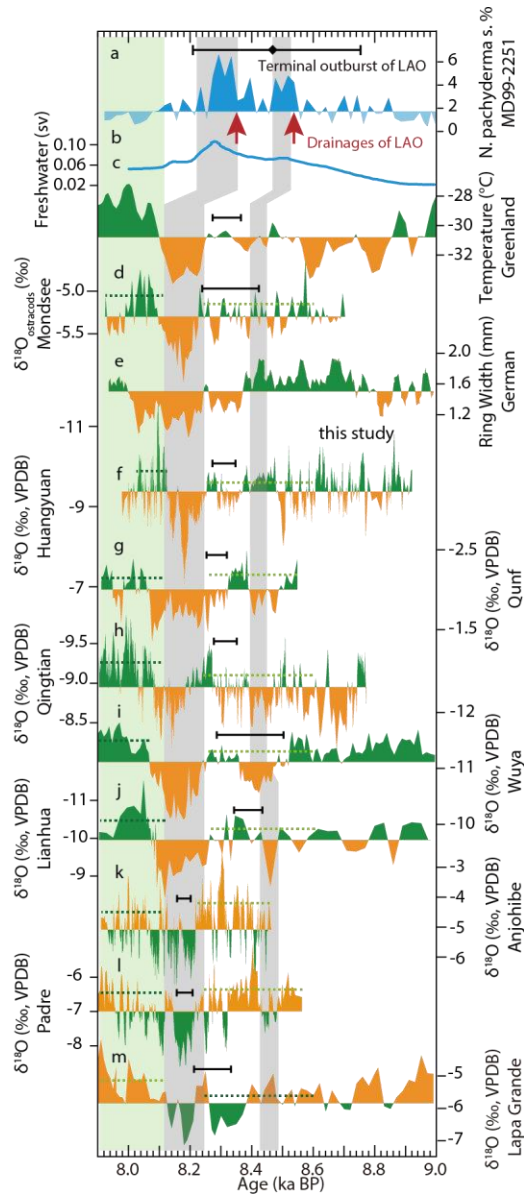
Figure 3. Comparisons of the BH-2 $\delta^{18}O$ record with records from circum-North Atlantic, ASM domain and

South America. (**a**) *N.pachydermas.abundance* record from MD03-2665, North Atlantic (Ellison et al., 2006). The

black diamond and error bar on the top indicate the dating of terminal outburst of LAO (Barber et al., 1999). The

red arrows point to the two-step drainages of LAO into the North Atlantic. (**b**) Modelled freshwater flux from Laurentide

Ice Sheet in unit of Sverdrups (Sv) (Matero et al., 2020). (**c**) Reconstructed temperature in Greenland (Kobashi et al.,

2017). (**d**) $\delta^{18}O_{ostracods}$ record from Modesee, Austria (Andersen et al., 2017). (**e**) Ring width of tree from Germany

(Spurk et al., 2002). (**f**) The BH-2 $\delta^{18}O$ record from Huangyuan Cave, Beijing (this study). (**g**) High-resolution $\delta^{18}O$

record (Fleitmann et al., 2003) from Qunf Cave with more precise ages (Cheng et al., 2009) (**h**) $\delta^{18}O$ record from

Qingtian Cave, China (Liu et al., 2015). (**i**) $\delta^{18}O$ record from Wuya Cave, Northwest China (Tan et al., 2020). (**j**) $\delta^{18}O$

record from Lianhua Cave, North China (Dong et al., 2018). (**k**) $\delta^{18}O$ record from Anjohibe Cave, Northwest

Madagascar (Duan P et al., 2021). (**l**) High-resolution $\delta^{18}O$ record from Padre Cave, Brazil, on the Oxcal-derived

684   chronology based on the ^{230}Th dates of Cheng et al. (2009). (**m**) High-resolution δ^{18}O record from Lapa Grande Cave,

685   Brazil (Stríkis et al., 2011). The δ^{18}O scale of **k**–**m** is inverse to other speleothem records. The vertical gray shading

686   bars indicate the events centered at 8.5 and 8.2 ka BP and the green shading bar marks the post-8.2 ka evnet. The δ^{18}O

687   value lower than the mean value of the entire records from the Northern Hemisphere, and Greenland reconstructed

688   temperature record higher than the mean value of the entire record is shaded in green. The δ^{18}O values higher than the

689   mean value of the entire records from the Southern Hemisphere are shaded in brown. The green horizontal dashed

690   lines in each record indicate the mean δ^{18}O values for the age range they cover before (8.60–8.22 ka BP) and after

691   (8.10–7.90 ka BP) the 8.2 ka event. The typical error of dating are shown as black bar in each curve.